LASER PHYSICS LETTERS

www.lphys.org

Abstract: Ultrafast two dimensional infrared (2D-IR) vibrational echo spectroscopy has emerged as a powerful method for the study of molecular dynamics under thermal equilibrium conditions occurring on ultrafast time scales. Here, we describe experimental details of 2D-IR vibrational echo spectroscopy including the experimental setup, pulse sequence, heterodyne detection, and extraction of the mainly absorptive part of the 2D-IR spectrum. As an experimental example, the measurements of the hydrogen bond dynamics of neat water and water in a high concentration of NaBr solution are presented and compared. The experiments are performed on OD stretching vibration of dilute HOD in H_2O to eliminate contributions from vibrational excitation transport. A new experimental observable for extracting dynamical information that yields the frequency-frequency correlation function is presented. The observable is the inverse of the center line slope (CLS) of the 2D spectrum, which varies from a maximum of 1 to 0 as spectral diffusion proceeds. The CLS is the inverse of the slope of the line that connects the maxima of the peaks of a series of cuts through the 2D spectrum that are parallel to the frequency axis associated with the first radiation field-matter interaction. Comparisons of the dynamics obtained from the data on water and the concentrated NaBr solutions show that the hydrogen bond dynamics of water around ions are much slower than in bulk water.

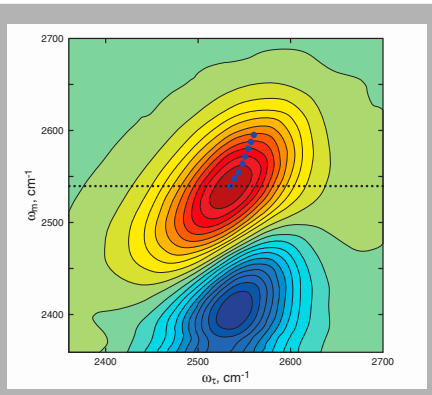

2D-IR spectrum at $T_w = 0.2$ ps. A dotted horizontal line defines a frequency slice at $\omega_m = 2540$ cm^{-1} along the ω_τ axis

Ultrafast 2D-IR vibrational echo spectroscopy: a probe of molecular dynamics

S. Park, K. Kwak, and M.D. Fayer

Department of Chemistry, Stanford University, Stanford, California 94305, USA

Received: 19 April 2007, Accepted: 25 April 2007
Published online: 9 May 2007

Laser Phys. Lett. **4**, No. 10, 704–718 (2007) / **DOI** 10.1002/lapl.200710046

WILEY-VCH

Laser Phys. Lett. **4**, No. 10, 704–718 (2007) / **DOI** 10.1002/lapl.200710046

Abstract: Ultrafast two dimensional infrared (2D-IR) vibrational echo spectroscopy has emerged as a powerful method for the study of molecular dynamics under thermal equilibrium conditions occurring on ultrafast time scales. Here, we describe experimental details of 2D-IR vibrational echo spectroscopy including the experimental setup, pulse sequence, heterodyne detection, and extraction of the mainly absorptive part of the 2D-IR spectrum. As an experimental example, the measurements of the hydrogen bond dynamics of neat water and water in a high concentration of NaBr solution are presented and compared. The experiments are performed on OD stretching vibration of dilute HOD in H_2O to eliminate contributions from vibrational excitation transport. A new experimental observable for extracting dynamical information that yields the frequency-frequency correlation function is presented. The observable is the inverse of the center line slope (CLS) of the 2D spectrum, which varies from a maximum of 1 to 0 as spectral diffusion proceeds. The CLS is the inverse of the slope of the line that connects the maxima of the peaks of a series of cuts through the 2D spectrum that are parallel to the frequency axis associated with the first radiation field-matter interaction. Comparisons of the dynamics obtained from the data on water and the concentrated NaBr solutions show that the hydrogen bond dynamics of water around ions are much slower than in bulk water.

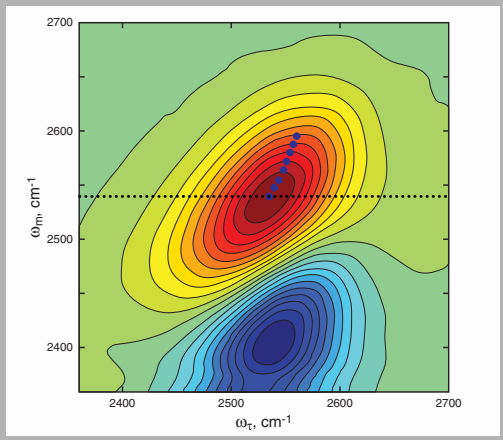

2D-IR spectrum at $T_w = 0.2$ ps. A dotted horizontal line defines a frequency slice at $\omega_m = 2540$ cm^{-1} along the ω_τ axis

Ultrafast 2D-IR vibrational echo spectroscopy: a probe of molecular dynamics

S. Park, K. Kwak, and M.D. Fayer *

Department of Chemistry, Stanford University, Stanford, California 94305, USA

Received: 19 April 2007, Accepted: 25 April 2007
Published online: 9 May 2007

Key words: two dimensional infrared vibrational echo spectroscopy; frequency-frequency correlation function; third-order four wave mixing; heterodyne detection; spectral diffusion; hydrogen bond

PACS: 78.47.+p, 82.53.Kp, 82.53.Uv

1. Introduction

Over the last decade, ultrafast multidimensional nonlinear spectroscopies with multiple visible [1] and infrared (IR) pulses [2–4] have been developed and have combined with rapid advances in ultrashort and high power laser technology to reveal the dynamics of complex molecular systems that previously could not be studied by one-dimensional (1D) spectroscopic methods. Molecular dynamics on subpicosecond and picosecond time scales are measured in the multidimensional nonlinear spectroscopy by manipulating the sequences of ultrashort femtosecond pulses and examining the nonlinear response of the system as a function of the timing between the pulses.

Ultrafast two dimensional IR (2D-IR) vibrational echo spectroscopy is an ultrafast IR experimental method that is

* Corresponding author: e-mail: fayer@stanford.edu

in some respects akin to 2D NMR [5], but it probes molecular vibrations instead of nuclear spins [5]. 2D-IR vibrational echo methods are an important development that follows the first ultrafast 1D-IR vibrational echo experiments conducted over a decade ago [6]. Vibrations are the mechanical degrees of freedom of molecules and thus are sensitive to molecular dynamics of molecular structure and intermolecular interactions. As opposed to electronic excitations, the vibrational excitations in 2D-IR vibrational echo spectroscopy produce a negligible perturbation of a molecular system with less energetic IR photons. In contrast to the electronic excitation, a vibrational excitation does not change the chemical properties of the molecular system under study [7,8]. In general, 2D-IR vibrational echo spectroscopy can be used to study molecular systems under a thermal equilibrium condition and measure molecular dynamics occurring on subpicosecond to picosecond time scales [2,4,7–25]. 2D-IR vibrational echo spectroscopy has been applied to study chemical exchange reactions [2,3,24], molecular internal rotation dynamics [4], water dynamics [17,22,23], hydrogen bond dynamics of alcohols [16,26], vibrational population transfer [27], intramolecular vibrational coupling [28], and mixed chemical analysis [29]. An increasing number of research groups are applying 2D-IR spectroscopy to the study of biological problems [8,11,18,25,30–42]. The applications of 2D-IR vibrational echo spectroscopy are increasing rapidly in areas of physics, chemistry, biology, and materials science.

2D-IR vibrational echo spectroscopy involves three IR pulses that excite molecular vibrations, and because of nonlinear radiation field-matter interactions, the fourth IR pulse is emitted, the vibrational echo, which is the signal in the experiment. The first IR pulse excites the molecules to a coherence state where their wavefunctions are superpositions of the $v = 0$ and $v = 1$ energy levels. In effect, the first interaction causes the molecules to "oscillate" in phase at their initial frequencies. The phase relationships among the molecules decay quickly because of static inhomogeneous and dynamic broadening mechanisms. The decay of the phase relationships produces a vibrational free induction decay (FID). The second IR pulse transfers the coherence state into a population state in either v = 0 or v = 1 energy level, depending on the phase of the particular molecule at the time of the pulse. During the population period, the molecules can undergo spectral diffusion, that is, their frequencies evolve because of dynamic structural evolution of the system. Spectral diffusion causes molecules to lose memory of their initial frequencies. In the water systems discussed below, time dependent evolution of water's hydrogen bond network causes spectral diffusion of the hydroxyl stretching vibration of water because the stretching vibration frequency is sensitive to the strength and number of hydrogen bonds [16,17]. Other processes called chemical exchange, in which the initial frequency makes a sudden jump because a molecule undergoes an abrupt change in its intra- or intermolecular chemical structure, can also occur during the population period [2,4,7,24]. The third IR pulse brings the molecules to a second coherence state where their wavefunctions are again superpositions of $v = 0$ and $v = 1$ energy levels or between $v = 1$ and $v = 2$ energy levels. As in an NMR spin echo, the phase relationships lost during the first FID can be restored, with the result that a macroscopic oscillating electric dipole is generated. This oscillating dipole gives rise to the emission of the vibrational echo pulse. The phase relationships are again lost via a second FID. The vibrational echo is overlapped spatially and temporally with another pulse, the local oscillator. The combined vibrational echo and local oscillator pulse is detected. The local oscillator, through the heterodyne detection, provides a phase reference so that both intensity and phase information are obtained from the vibrational echo pulse. During the second coherence period (time between the third pulse and the vibrational echo emission), the molecules oscillate at their final frequencies, which can be different from those they had during the first coherence period (time between pulses 1 and 2).

In short, during the first coherence period, the molecules are frequency-labeled. During the population period, the frequency-labeled molecules can evolve to different frequencies (spectral diffusion) because of microscopic molecular events. During the second coherence period, the final frequencies of the frequency-labeled molecules are read out. A 2D correlation map (spectrum) is obtained with the initial labeled frequencies as one axis in the 2D spectrum and the final frequencies of the molecules as the other axis. The time between pulses 1 and 2 is τ and the time between pulses 2 and 3 is T_w. The vibrational echo pulse is generated after pulse 3 at a time $\leq \tau$. 2D vibrational echo spectra are obtained by scanning τ at fixed T_w. A set of such 2D spectra is obtained as a function of T_w. By analyzing the amplitudes, positions, and peak shapes of the 2D spectra, detailed information on structure and dynamics of the molecular system is obtained. Spectral diffusion results in changes in peak shapes as a function of T_w [17,43]. Appearance of off-diagonal peaks results from incoherent and coherent population transfers by anharmonic interactions [27,44] or chemical exchange [2]. Off-diagonal peaks occurring at $T_w = 0$ can arise from state coupling of different vibrational modes [45]. Vibrational population relaxation and molecular reorientation lead to decay of the amplitudes of all peaks [7,8,15].

The paper is organized as follows. A brief theoretical background of the ultrafast 2D-IR vibrational echo experiment is given in Sec. 2. Details of the 2D-IR vibrational echo experiment are presented in Sec. 3 including the experimental setup, data acquisition method, and "phasing" process required to obtain essentially absorptive 2D spectra. In Sec. 4, new 2D-IR vibrational echo experiments comparing the dynamics of water and a concentrated NaBr salt solution are discussed. The inverse of the center line slope (CLS) is defined as a new experimental observable in 2D vibrational spectra that is useful for quantifying spectral diffusion dynamics. Sec. 5 presents some concluding remarks.

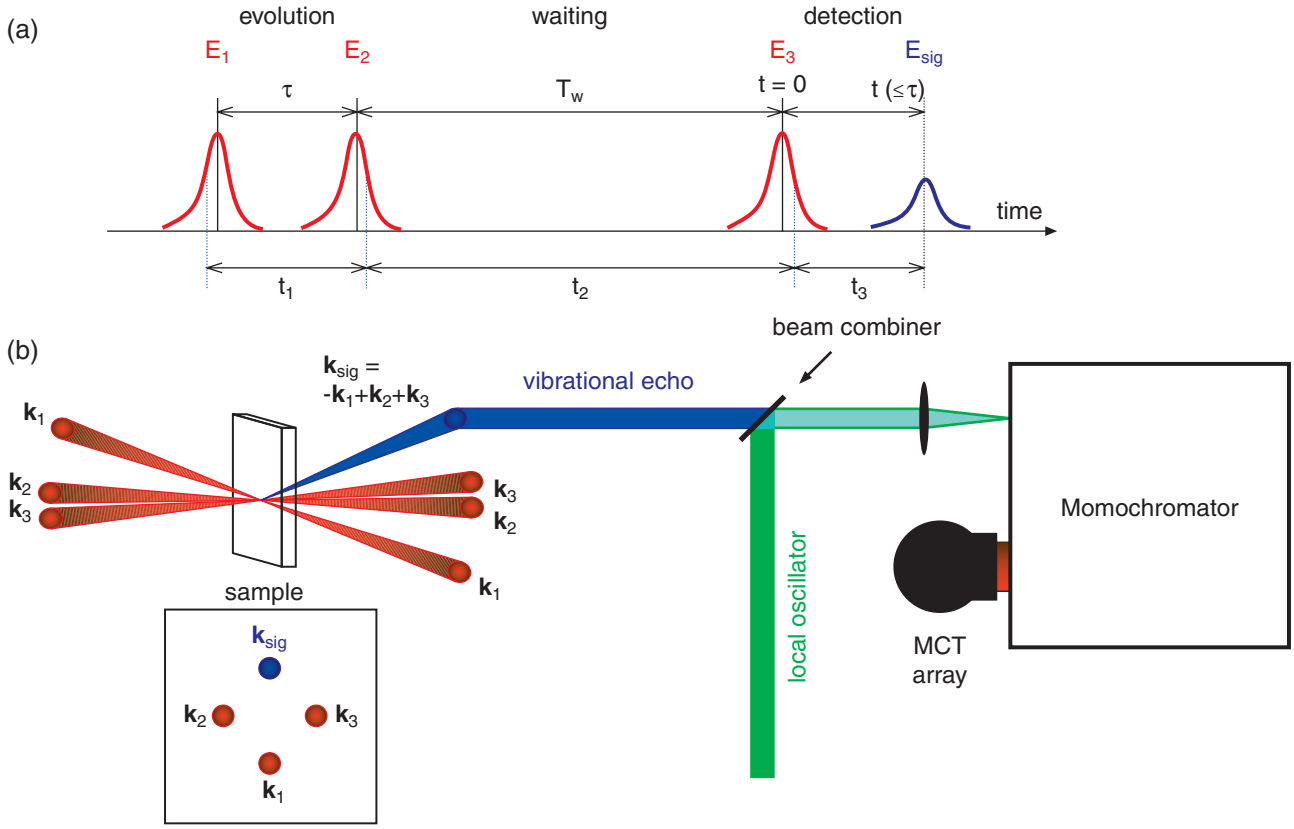

Figure 1 (online color at www.lphys.org) (a) – 2D-IR vibrational echo pulse sequence with the time variables (t_1, t_2, and t_3) of field-matter interactions, pulse sequence ($\mathbf{E}_1$, $\mathbf{E}_2$, and $\mathbf{E}_3$), experimental time variables (τ, T_w, and t), time periods (evolution, waiting, and detection). Time flows from left to right. (b) – schematic of the non-collinear excitation beam geometry, phase-matched direction, and heterodyne detection of the vibrational echo signal in 2D-IR experiments

2. Theoretical background

The 2D-IR vibrational echo experiment is a nonlinear four wave mixing spectroscopy involving three input IR electric fields in a non-collinear beam geometry [15,46–48]. Fig. 1 illustrates the sequence of three field-matter interactions, experimental time variables, time periods, non-collinear beam geometry, and phase-matched condition. The system is initially in thermal equilibrium before any field-matter interactions. The frequency of the IR pulse is tuned to the transition frequency of the vibrational mode or modes of interest. Because the pulse is very short, its band width can span a number of modes of a very broad band such as that associated with the hydroxyl stretching vibrational mode of water. After the first field-matter interaction, the molecular vibrational modes are in coherence states oscillating with initial vibrational transition frequencies (0-1). The second field-matter interaction brings the system to population states, either the ground state (0) or the first vibrationally excited state (1). Following the third field-matter interaction, the molecules are again in a coherence state oscillating with their final transition frequencies. The signal field is radiated with those final transition frequencies in the wave vector phase-matched direction and is combined with a local oscillator (LO) for heterodyne detection. There are three time periods in the experiment: evolution (τ), waiting (T_w), and detection (t) as shown in Fig. 1a. To obtain the 2D-IR spectra in the frequency domain, two Fourier transforms are required. One is done experimentally when the monochromator spectrally resolves the signal-local oscillator pulse. This transform gives the ω_m axis corresponding to the time variable t. When τ is scanned, an interferogram is obtained at each ω_m. These interferograms are numerically Fourier transformed to provide the ω_τ axis. The details of these procedures are discussed below. In the 2D-IR vibrational echo experiment, 2D frequency correlation maps (spectra) between the evolution and detection time periods are obtained as a function of waiting time (T_w), which provides direct information on the time evolution of the molecular system.

In third-order four wave mixing experiments, three input electric fields ($\mathbf{E}_1$, $\mathbf{E}_2$, and $\mathbf{E}_3$ each with a unique wave vector $\mathbf{k}_1$, $\mathbf{k}_2$, and $\mathbf{k}_3$, respectively) interact with

a system and create a third-order nonlinear polarization $\mathbf{P}^{(3)}$ that subsequently radiates a signal field $\mathbf{E}_{sig}$ in the $\mathbf{k}_{sig} = -\mathbf{k}_1+\mathbf{k}_2+\mathbf{k}_3$ phase-matched direction. The third-order nonlinear polarization is expressed as time ordered integrals of a response function $\mathbf{R}^{(3)}(t_3, t_2, t_1)$ and three input fields $\mathbf{E}(\mathbf{k})$ [46]. The radiated signal field is written as [46]

$$\mathbf{E}_{sig}(\mathbf{k}_{sig}, t) \propto i\mathbf{P}^{(3)}(\mathbf{k}_{sig}, t) = \tag{1}$$

$$= \int_0^\infty dt_3 \int_0^\infty dt_2 \int_0^\infty dt_1 \mathbf{R}^{(3)}(t_3, t_2, t_1)\mathbf{E}_3(\mathbf{k}_3, t - t_3)\times$$

$$\times \mathbf{E}_2(\mathbf{k}_2, t - t_3 - t_2)\mathbf{E}_1(\mathbf{k}_1, t - t_3 - t_2 - t_1)\,.$$

The response function is a nested commutator of the transition dipole operator $\boldsymbol{\mu}(t)$ that is evaluated at the time point of the field-matter interactions [15]

$$\mathbf{R}^{(3)}(t_3, t_2, t_1) = \tag{2}$$

$$= \left(\frac{i}{\hbar}\right)^3 \langle[[[\boldsymbol{\mu}(t_3 + t_2 + t_1), \boldsymbol{\mu}(t_2 + t_1)], \boldsymbol{\mu}(t_1)], \boldsymbol{\mu}(0)]\rangle\ .$$

The response function contains all of the information on the microscopic dynamics of the system because the dipole operator evolves under the system Hamiltonian H_o in the total Hamiltonian $H = H_o + H_{int}$ where H_{int} is the term for the interaction of the system with the radiation fields. H_{int} is evaluated in the perturbative limit using the rotating wave approximation (RWA). Therefore, only terms in the response function that are resonant with the electric fields are retained. Each term in the response function in the RWA represents a different density matrix pathway that depends on the sequence of field-matter interactions. Only terms that contribute to the signal in the phase-matched direction are included.

A three-level system is considered for the vibrational response function because the $v = 1 \rightarrow v = 2$ transition needs to be included as well as the fundamental transition ($v = 0 \rightarrow v = 1$) [15,47]. (The 1-2 transition comes into play for pathways that produce a population in the $v = 1$ level following the second pulse. The third pulse can then create a 1-2 coherence with subsequent vibrational echo emission at the 1-2 transition frequency, which differs from the 0-1 transition frequency by the anharmonic shift.) The response function can be separated into nonrephasing $\mathbf{R}^{(3)}_{NR}(t_3, t_2 t_1)$ and rephasing $\mathbf{R}^{(3)}_{R}(t_3, t_2, t_1)$ quantum pathways depending on the oscillation frequencies during the evolution and detection time periods. $\mathbf{R}^{(3)}_{NR}(t_3, t_2, t_1)$ pathways involve oscillations at the same frequency (same sign of the frequency) during both time periods, and thus they decay in time (nonrephasing). On the other hand, $\mathbf{R}^{(3)}_{R}(t_3, t_2, t_1)$ pathways can be "rephrased" because they involve oscillations during the detection time period with frequencies that are conjugate or nearly conjugate (opposite sign) to those during the evolution time period. The nonrephasing and rephasing signals are measured in the same phase-matched direction $\mathbf{k}_{sig} = -\mathbf{k}_1 + \mathbf{k}_2 + \mathbf{k}_3$ by changing the sequence of three input electric fields $\mathbf{E}_1(\mathbf{k}_1)$, $\mathbf{E}_2(\mathbf{k}_2)$, and $\mathbf{E}_3(\mathbf{k}_3)$. In the beam geometry shown in Fig. 1b, the nonrephasing signal $\mathbf{E}_{sig}(\mathbf{k}_{sig} = +\mathbf{k}_2 - \mathbf{k}_1 + \mathbf{k}_3)$ is measured with pulse sequence of $\mathbf{E}_2(\mathbf{k}_2)$, $\mathbf{E}_1(\mathbf{k}_1)$, and $\mathbf{E}_3(\mathbf{k}_3)$ while the rephasing signal $\mathbf{E}_{sig}(\mathbf{k}_{sig} = -\mathbf{k}_1 + \mathbf{k}_2 + \mathbf{k}_3)$ is obtained with $\mathbf{E}_1(\mathbf{k}_1)$, $\mathbf{E}_2(\mathbf{k}_2)$, and $\mathbf{E}_3(\mathbf{k}_3)$ [14].

When it is heterodyne detected, the vibrational echo signal is written with three experimental time variables by

$$S(\mathbf{k}_{sig}; \tau, T_w, t) \propto \mathbf{E}^*_{LO}(\mathbf{k}_{sig}) \cdot \mathbf{E}_{sig}(\mathbf{k}_{sig}; \tau, T_w, t)\,, \tag{3}$$

where $\mathbf{E}_{LO}(\mathbf{k}_{sig})$ is a time-independent local oscillator. Without heterodyne detection, the signal is proportional to $|\mathbf{E}_{sig}|^2$, and it contains no phase information. With the heterodyne detection method the signal $\mathbf{E}_{sig}(\mathbf{k}_{sig}; \tau, T_w, t)$ is linear in the electric field and amplified, giving full information on its amplitude, phase, and frequency. $\mathbf{E}_{sig}(\mathbf{k}_{sig}; \tau, T_w, t)$ has both absorptive and dispersive contributions. To obtain either pure or almost pure absorptive 2D vibrational echo spectra, which considerably narrows the spectra, nonrephasing and rephasing signals are separately collected by using different pulse sequences. These signals are Fourier transformed along both t-axis and τ-axis and are added [14]

$$S(\mathbf{k}_{sig}; \omega_\tau, T_w, \omega_m) = \tag{4}$$

$$= S_{NR}(\mathbf{k}_{sig}; \omega_\tau, T_w, \omega_m) + S_R(\mathbf{k}_{sig}; \omega_\tau, T_w, \omega_m)\,,$$

where $S_{NR}(\mathbf{k}_{sig}; \omega_\tau, T_w, \omega_m)$ and $S_R(\mathbf{k}_{sig}; \omega_\tau, T_w, \omega_m)$ are the nonrephasing and rephasing 2D spectra defined as

$$S_{NR}(\mathbf{k}_{sig}; \omega_\tau, T_w, \omega_m) = \tag{5}$$

$$= \mathrm{Re}\left[\int_0^\infty d\tau \int_0^\infty dt \exp[i\omega_m t + i\omega_\tau \tau] S_{NR}(\mathbf{k}_{sig}; \tau, T_w, t)\right]\,,$$

$$S_R(\mathbf{k}_{sig}; \omega_\tau, T_w, \omega_m) = \tag{6}$$

$$= \mathrm{Re}\left[\int_0^\infty d\tau \int_0^\infty dt \exp[i\omega_m t - i\omega_\tau \tau] S_R(\mathbf{k}_{sig}; \tau, T_w, t)\right]\,.$$

In practice, the t-axis in $S(\mathbf{k}_{sig}; \tau, T_w, t)$ is Fourier transformed during data collection by the monochromator and the τ-axis in $S(\mathbf{k}_{sig}; \tau, T_w, t)$ is numerically Fourier transformed after data acquisition is finished as described in more detail in the next section.

3. Experimental procedures

3.1. Femtosecond laser system and 2D-IR spectrometer

Femtosecond IR pulses employed in the experiments are generated using a Ti:Sapphire regeneratively amplified laser/OPA system. The output of a modified Spectra

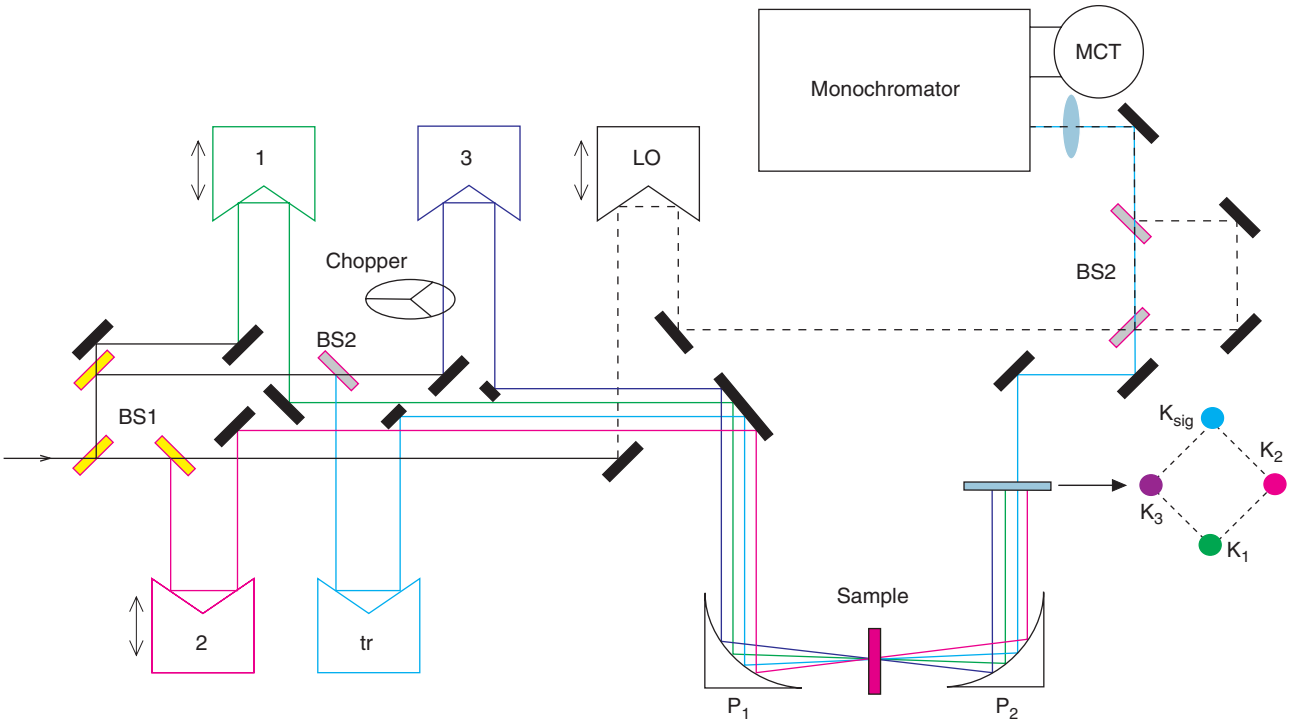

Figure 2 (online color at www.lphys.org) Schematic of 2D-IR spectrometer. Beam 1 (green), 2 (red), and 3 (purple) are the paths of the three excitation pulses. LO (black, dotted) and tr (blue) are a local oscillator and tracer, respectively. Following the sample, the vibrational echo pulse follows the same path as the tracer beam. Beam 1, 2, and LO are delayed by precision motorized translational stages (step size 10 nm) and their time delay positions are controlled by computer. BS1(yellow), 50:50 ZnSe beam splitters; BS2(light blue), ZnSe window; P1 and P2, 90° off-axis parabolic mirrors (3-inch in diameter and 15 cm in focal length); MCT, liquid N_2 cooled dual 2×32 element MCT array detector. The "diamond" at the right of the figure shows the non-collinear beam geometry and the phase-matched direction

Physics Regen is 30 fs transform-limited 0.6 mJ pulses centered at ∼ 800 nm with a 1 kHz repetition rate. These are used to pump an IR OPA to generate IR pulses μm in 0.5 mm thick $AgGaS_2$ crystal by difference frequency generation. For the experiments described below, the frequency is centered at 2510 cm^{-1}. The IR pulses are ∼ 55 fs transform-limited following compensation for chirp [16].

A schematic layout of the 2D-IR spectrometer is shown in Fig. 2. A HeNe laser beam (632 nm) is used to align all optics in the 2D-IR spectrometer. The IR beam is collimated allowing for propagation of several meters without significant divergence. A 2 mm thick Ge Brewster plate is used to overlap the IR beam with a mode-matched HeNe alignment beam. The IR beam passes through the plate and the HeNe reflects from it. 50:50 ZnSe beam splitters are used to split the IR beam into five beams. Three of them (denoted as 1 (red), 2 (green), and 3 (purple) in Fig. 2) are the excitation beams for the stimulated vibrational echo. The fourth beam (tr) is a tracer beam for alignment and is blocked during the 2D-IR experiment. All four beams are focused with a 3-inch diameter off-axis parabolic mirror (f.l. = 15 cm) in a diamond geometry as shown in Fig. 2 and are spatially overlapped at the sample position by having them go through a 100 μm pinhole. A fifth beam (LO, black dotted) does not go through the sample and is further split into a local oscillator and a reference beam. These two beams are dispersed in a monochromator (iHR320, Horiba) and are sent to the upper and lower 32 element stripes of a liquid N_2 cooled dual MCT (HgCdTe) array detector (Infrared Associates Inc.) with high speed data acquisition system (Infrared System Development Corp.), respectively. The vibrational echo signal is generated in the phase matched direction to the fourth corner of the diamond pattern shown in the figure (the tracer beam direction) and is temporally and spatially overlapped with the local oscillator for heterodyne detection. Beam 3 is chopped at 500 Hz to remove scattered light from the other excitation beams. It is important to chop beam 3. As discussed below, beams 1 and 2 are scanned to produce interferograms between the vibrational echo signal and the local oscillator. Scattered light from these beams will also produce interferograms.

However, beam 3 is fixed. Although scattered light from beam 3 will be heterodyne detected, it only produces a signal offset, which does not contribute to the Fourier transformed spectrum.

The chirp on excitation pulses is measured by a frequency resolved optically gating (FROG) method in a transient grating (TG) geometry [49]. By scanning pulse 2 with pulses 1 and 3 temporally overlapped, the homodyne TG signal of CCl_4 is measured and frequency-resolved. The frequency-resolved transients are fit to Gaussian functions to obtain the time zero position and width of the transient at each frequency. The plot of the time zero positions against frequency is a measure of chirp on the input pulses. CaF_2 plates with different thickness are used to balance the positive chirp introduced by other dielectric material in the setup, particularly the Ge Brewster plate, producing nearly transform-limited IR pulses at the sample position. The time zeros between excitation pulses are determined within $\pm$ 5 fs by iteratively scanning pulse 1 (or 2) with pulses 2 (or 1) and 3 overlapped and measuring a nonresonant TG signal of CCl_4. After the time zeros between excitation pulses are determined, the temporal and spatial overlap of the LO with the vibrational echo signal is checked by measuring a spectral interferogram between them. The nonresonant vibrational echo signal is generated by temporally overlapping three excitation pulses and is mixed with the LO pulse. The spatial overlap is maximized by increasing the depth of modulation in the spectral interferogram between the vibrational echo signal and the LO pulse by adjusting the mirrors steering the vibrational echo signal on top of the LO, which has previously be aligned through the monochromator onto the two array stripes. Inverse Fourier transformation of the spectral interferogram converts the fringe spacing into the corresponding temporal separation so that the LO pulse can be moved temporally and placed on top of pulse 3 within $\pm$ 5 fs.

Prior to the monochromator, the LO is split into two. One beam is combined with the vibrational echo, passed through the monochromator, and detected by the upper MCT array stripe. The other beam is used as a reference beam. It is passed through the monochromator and detected by the lower array stripe. 32 pixel frequencies in the MCT array were calibrated by using a spectral interferogram between the LO and tracer pulses. The LO and tracer pulses were spatially overlapped and shifted temporally by a few picoseconds to produce a spectral interferogram on the MCT array detector. The same spectral interferogram was measured through a slit at a different exit port of the monochromator with a single element MCT detector by scanning the monochromator. Corrections to the array detected spectrum were made to make it correspond to the scanned spectrum.

3.2. Data acquisition

In 2D-IR vibrational echo spectroscopy, the vibrational echo signal was measured as a function of one frequency variable, ω_m, and two time variables, τ and T_w. τ is defined by the time between the first and second IR pulses and T_w is the time between the second and third IR pulses. The monochromator performs an experimental Fourier transform to give the ω_m frequency axis. The heterodyne detected signal is given by

$$|\mathbf{E}_{sig}(t) + \mathbf{E}_{LO}|^2 = \tag{7}$$

$$= |\mathbf{E}_{LO}|^2 + |\mathbf{E}_{sig}(t)|^2 + 2\mathbf{E}_{sig}(t) \cdot \mathbf{E}^*_{LO} \,.$$

$|\mathbf{E}_{LO}|^2$ is a time-independent constant offset. The homodyne signal $|\mathbf{E}_{sig}(t)|^2$ is negligibly small since $\mathbf{E}_{LO} \gg \mathbf{E}_{sig}(t)$ is set in the experiment. In addition, it is a slowly varying envelope and does not contribute to the Fourier transform of the interferogram. The third term is the heterodyne signal. As discussed above, pulse 3 is chopped at 500 Hz. In the dual array configuration, the signal is recorded as

$$\mathbf{S}(t) = \frac{\mathbf{S}_{open}(t)}{\mathbf{S}_{close}(t)} - 1 = \tag{8}$$

$$= \frac{|\mathbf{E}_{sig}(t) + \mathbf{E}_{LO}|^2_{upper}}{|\mathbf{E}_{ref}|^2_{lower}} \cdot \frac{|\mathbf{E}_{ref}|^2_{lower}}{|\mathbf{E}_{LO}|^2_{upper}} - 1 \propto$$

$$\propto 2\,\mathbf{E}_{sig}(t) \cdot \mathbf{E}^*_{LO} \,.$$

$\mathbf{S}_{open}(t)$ and $\mathbf{S}_{close}(t)$ are the signals measured with a chopper open and closed, respectively. $\mathbf{E}_{ref}$ represents a reference beam sent to the lower stripe of the dual array. $\mathbf{E}_{ref} = \mathbf{E}_{LO}$ when the dual array is normalized.

In a dual MCT 2×32 array configuration with upper and lower stripes, the LO and reference beams are sent to the upper and lower stripes, respectively. First, 32 pixels in the upper stripe are normalized so that each pixel gives the same responsivity. 32 pixels in the lower stripe are normalized to the corresponding 32 pixels in the upper stripe. In this normalization scheme, the lower stripe works identically as the upper stripe if there is no pixel noise. However, the pixel noise is much smaller than shot-to-shot laser intensity fluctuations. As a result, the dual array configuration effectively reduces the shot-to-shot spectral noise arising from instability of the generated IR pulses and improves the signal-to-noise ratio. At each monochromator setting, the dual array detects 32 individual frequencies at the same time.

As τ is scanned at a fixed T_w, the phase of the vibrational echo signal field is scanned relative to the fixed LO field, resulting in an interferogram as a function of τ. The interferograms contain full information on the amplitude, sign, frequency, and phase of the vibrational echo signal field. The interferograms obtained at given monochromator frequencies are numerically Fourier transformed to the frequency domain to give the ω_τ axis.

The interferogram measured as a function of τ contains both the absorptive and dispersive parts of the vibrational echo signal. To obtain the pure or nearly pure absorptive part of the vibrational echo signal, a dual scan method is used [14]. As explained in Sec. 2, there are two sets of quantum pathways (nonrephasing and rephasing) depending on the phase relation of the signal between the

evolution and detection period. Nonrephasing and rephrasing signals can be measured separately by changing the sequence of excitation pulses in the 2D-IR vibrational echo experiment [14]. In the beam geometry shown in Fig. 1, the nonrephasing signal is obtained if pulse 2 precedes pulse 1 whereas the rephasing signal is obtained if pulse 1 precedes pulse 2. The dispersive parts of the nonrephasing and rephrasing signals are 180 out of phase while the absorptive parts of them are in-phase. Adding the nonrephasing and rephrasing signals, the dispersive parts are cancelled, leaving only the absorptive part. Nonrephasing and rephasing interferograms at a monochromator frequency are shown in Fig. 3a for OD hydroxyl stretching vibration of dilute HOD in H_2O. The experimental results are discussed in detail below. The nonrephasing interferogram was obtained by scanning pulse 2 from a negative time to the time zero (where pulse 1 is located) while the rephasing interferogram was measured by scanning pulse 1 from the time zero to a positive time.

3.3. Phasing 2D vibrational echo spectra

As mentioned above, there is an experimental uncertainty in determining the time zeros between excitation pulses, compensating the chirp of the excitation pulses, and considering the chirp on the emitted vibrational echo pulse. These experimental factors distort the spectral phase in the absorptive 2D correlation spectra. To get a correct absorptive 2D spectrum, the spectral phase needs to be adjusted, i.e., a "phasing" procedure must be employed [16,43]. The projection slice theorem is employed to correct the spectral phase to obtain the absorptive 2D spectrum [14–17,22,23,43,50,51]. The projection of the 2D spectrum onto the ω_m axis is equal to the IR pump-probe spectrum measured at the same T_w, as long as all of the contributions to the vibrational echo are purely absorptive. Numerical adjustments are made that compensate for timing errors and chirp using the theoretical approach that has been described previously [16]. The spectral phase of the 2D correlation spectrum is very sensitive to small errors in the time origin, even on the order of 1 fs, and to chirp. The frequency-dependent phasing factor used to adjust the spectral phase in the 2D correlation spectra has the form

$$S_C(\omega_m,\omega_\tau) = S_{NR}(\omega_m,\omega_\tau)\exp\left[i\phi_{NR}(\omega_m,\omega_\tau)\right] + \quad (9)$$

$$+S_R(\omega_m,\omega_\tau)\exp\left[i\phi_R(\omega_m,\omega_\tau)\right] ,$$

$$\phi_{NR}(\omega_m,\omega_\tau) = \quad (10)$$

$$= -\omega_\tau\Delta\tau_{1,2} + \omega_m\Delta\tau_{3,LO} + \omega_m\omega_\tau Q_1 + \omega_m^2\omega_\tau^2 Q_2 ,$$

$$\phi_R(\omega_m,\omega_\tau) = \quad (11)$$

$$= \omega_\tau\Delta\tau_{1,2} + \omega_m\Delta\tau_{3,LO} + \omega_m\omega_\tau Q_1 + \omega_m^2\omega_\tau^2 Q_2 .$$

$S_C(\omega_m,\omega_\tau)$ is the phased 2D correlation spectrum. $S_{NR}(\omega_m,\omega_\tau)$ and $S_R(\omega_m,\omega_\tau)$ are the nonrephasing and rephasing 2D spectra, respectively. $\Delta\tau_{1,2}$ is the uncertainty of time zero between the excitation pulses 1 and 2, while $\Delta\tau_{3,LO}$ accounts for the time zero error between the excitation pulse 3 and the LO. The third and fourth terms in $\phi_{NR}(\omega_m,\omega_\tau)$ and $\phi_R(\omega_m,\omega_\tau)$ are correction factors for chirp on excitation pulses and the vibrational echo pulse. Note that $\Delta\tau_{1,2}$ comes in with opposite sign for nonrephasing and rephasing 2D spectra. The four parameters, $\Delta\tau_{1,2}$, $\Delta\tau_{3,LO}$, Q_1, and Q_2, are adjusted until the projected 2D spectrum matches the pump-probe spectrum.

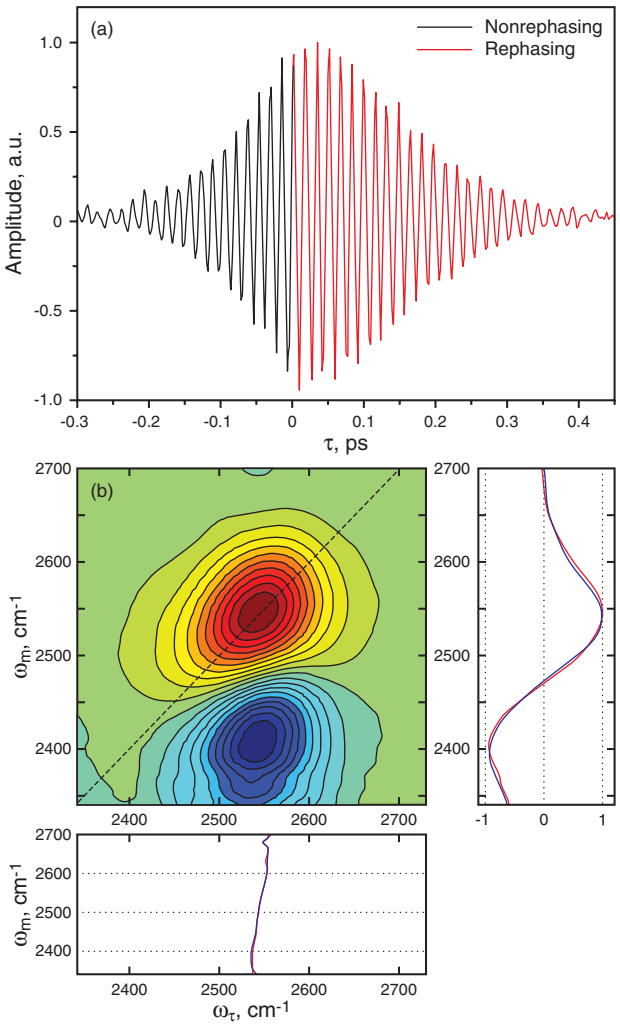

Figure 3 (online color at www.lphys.org) (a) – nonrephasing and rephasing interferograms at a single monochromator frequency measured by the dual phase scan method. (b) – absorptive 2D-IR vibrational echo spectrum obtained by using a phasing procedure with the projection slice theorem (right panel) along the ω_m axis and the center of gravity lines (lower panel) along the ω_τ axis. In the right panel, the blue line is the pump-probe spectrum and the red line is the projection of 2D spectrum onto the ω_m axis. In the lower panel, the two types of center of gravity lines. See the text for details. The dashed line is the diagonal

In most instances, it is possible to obtain essentially the correct 2D spectrum using only the projection theorem procedure. In many situations in which the peaks in the 2D spectra are relatively narrow, and particularly if the amplitudes and positions of the peaks are all that is required, the projection theorem is sufficient for phasing the 2D spectrum [14,15,22,23,50–52]. However, for the very broad water spectrum discussed below, in which very accurate T_w dependent shapes of the 2D spectra are required, to adjust the spectral phase unambiguously, it is preferable to have constraints on both ω_m axis and ω_τ axis. Therefore, an additional constraint is applied for the ω_τ axis in the phasing procedure. The absolute value nonrephasing $|S_{NR}(\omega_m,\omega_\tau)|$ and rephasing $|S_R(\omega_m,\omega_\tau)|$ spectra, which are independent of the phase factors $\phi_{NR}(\omega_m,\omega_\tau)$ and $\phi_R(\omega_m,\omega_\tau)$, are projected onto the ω_τ axis. The peaks of these two spectra are at the same frequency along the ω_τ axis. This should be also true for the purely absorptive 2D correlation spectra. The projected spectrum of $|S_C(\omega_m,\omega_\tau)|$ onto the ω_τ axis is dependent on $\phi_{NR}(\omega_m,\omega_\tau)$ and $\phi_R(\omega_m,\omega_\tau)$, because of the cross term in Eq. (9). Peak positions in the projected spectrum of $|S_{NR}(\omega_m,\omega_\tau)|+|S_R(\omega_m,\omega_\tau)|$ onto the ω_τ axis should be the same as the projected spectrum of $|S_C(\omega_m,\omega_\tau)|$ onto the ω_τ axis when $S_C(\omega_m,\omega_\tau)$ is properly phased. This peak position matching along the ω_τ axis is self-contained because the same nonrephasing and rephrasing spectra measured in 2D-IR experiments are used while the projection slice theorem requires pump-probe spectra measured separately. By putting these two constraints along both the ω_m axis and ω_τ axis and using a nonlinear fitting algorithm, the four parameters $\Delta\tau_{1,2}$, $\Delta\tau_{3,LO}$, Q_1, and Q_2 in Eqs. (10) and (11) are varied to obtain the correct absorptive 2D spectrum [16,25,43]. This method is quite general and can be applied to phase 2D correlation spectra having multiple peaks along the ω_τ axis.

When 2D vibrational echo spectrum has only one 0-1 peak and the corresponding 1-2 peak along the ω_τ axis, as is the case of water, a "center of gravity" line can be used as a very strong constraint for the ω_τ axis. The peak positions of slices along ω_τ at all ω_m frequencies of the $|S_{NR}(\omega_m,\omega_\tau)|+|S_R(\omega_m,\omega_\tau)|$ spectrum (absolute value spectrum) and the $|S_C(\omega_m,\omega_\tau)|$ spectrum (absolute value of the absorptive 2D spectrum) are determined. The plot of ω_τ peak frequencies vs. ω_m is the center of gravity line [16,17,43]. An example is shown in Fig. 3b. A 2D vibrational echo spectrum is of the OD stretching vibration of 5% HOD in H_2O in a high concentration NaBr solution at $T_w = 1.5$ ps. The dashed line is the diagonal. The peak on the diagonal is from the 0-1 transition. It is positive going. The off-diagonal peak is negative going. It results from vibrational echo emission at the 1-2 transition frequency. It is shifted along the ω_m axis by the anharmonicity of the OD stretching vibration. To the right of the 2D spectrum are the pump-probe spectrum (blue) and the projection of the 2D spectrum (red). Below the 2D spectrum are the center of gravity lines of the absolute value spectrum (blue) and the absolute value of the absorptive 2D spectrum (red). The projected and pump-probe spectra in the right panel and the center of gravity lines in the lower panel in Fig. 3b show excellent agreement, demonstrating that the 2D vibrational echo spectrum is properly phased.

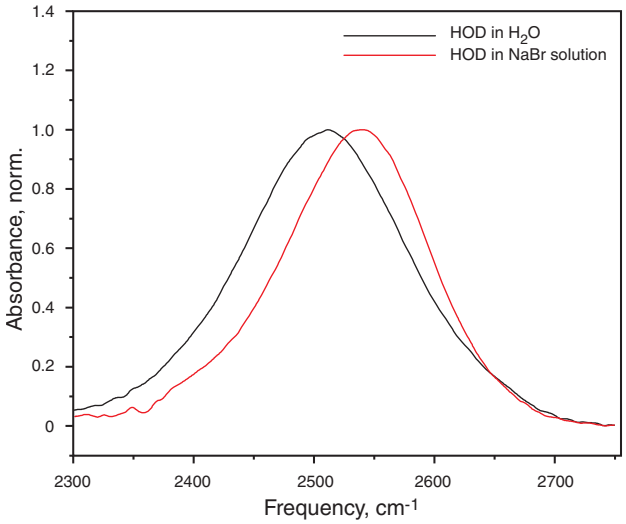

Figure 4 (online color at www.lphys.org) FT-IR absorption spectra of 5% HOD in H_2O (neat water) and in NaBr:H_2O=1:8 solution. The H_2O background is subtracted

3.4. Sample preparation and 2D-IR vibrational echo measurements

D_2O was purchased from Sigma-Aldrich and used as received. 5% of HOD in H_2O solution was prepared by adding 2.5 wt.% of D_2O to H_2O. A NaBr:H_2O = 1:8 solution was prepared by mixing 0.1 mol of NaBr salt with 0.8 mol of 5% of HOD in H_2O. Samples were placed in a cell with two 3 mm thick CaF_2 windows. The optical path length was set with a 6 μm thick Teflon spacer. Optical densities of the two samples at peaks at $\sim$ 2500 cm^{-1} (OD stretching vibration) were less than 0.3 including the $\sim$ 0.1 H_2O background absorption. Absorption spectra of the samples were measured before and after 2D-IR vibrational echo experiments. There were no changes in absorption spectra. Normalized absorption spectra of two samples are shown in Fig. 4. The IR pulses were centered at 2520 cm^{-1} with a bandwidth of $\sim$ 250 cm^{-1} FWHM. Frequency resolution of each pixel in the MCT array was 5–7 cm^{-1} depending on the recorded frequency. Two array blocks (64 pixels) were used to scan the spectral range of 2340 to 2700 cm^{-1}. The IR portion of the 2D-IR setup was purged with dry air during the experiment to eliminate CO_2 and H_2O. The time zeros between excitation pulses were checked before and after measurements to make sure that there was no time zero drift. After the 2D-IR vibrational echo experiments were finished, the 2D-

IR setup was reconfigured to a pump-probe setup. Pump-probe spectra were measured at all T_w times and used for phasing of the 2D spectra.

4. The effect of concentrated NaBr salt on water dynamics

Water plays an important role in chemistry, biology, geology, and materials science. It is a solvent for a wide variety of molecules and compounds, and it is a particularly good solvent for ionic compounds because of its high dielectric constant. Water dissolves ions by ion-dipole interactions. Because of the large electronegativity of oxygen, the oxygen atom in water carries a partial negative charge while the hydrogens carry partial positive charges. Thus, schematically for a negative ion, HOH-Y^-, where, for example, Y = F, Cl, Br, or I, and for a positive ion, H_2O-X^+, with, for example, X = Na or K. The structure and dynamics of water molecules around ions are of fundamental importance in understanding ionic solvation and chemical reactions involving charged species in aqueous solutions. Vibrational population relaxation and orientational relaxation dynamics of water in bulk [53,54], nanoscopic environments [55–58], and ionic solutions [59–61] have been extensively studied by femtosecond IR pump-probe experiments. Vibrational echo experiments on hydroxyl stretching vibration have explicated the dynamics of hydrogen bond network in bulk water. Vibrational echo peak shift measurements [62–65] and 2D-IR vibrational echo spectroscopy experiments [17,22,23,43] combined with molecular dynamics simulations [66–75] have revealed detailed information on the nature of structural evolution of hydrogen bond network of bulk water. The results have shown that the dynamics of water responsible for spectral diffusion observed in the experiments occur over time scales ranging from sub-100 fs to picoseconds. The fastest dynamics are associated with very local hydrogen bond fluctuations. The longest time scale dynamics involve global structural rearrangement of hydrogen bond network that completes the randomization of hydrogen bond structures and the sampling of all frequencies in the absorption spectrum of hydroxyl stretching vibration (complete spectral diffusion).

Here the results of initial 2D-IR vibrational echo experiments used to study spectral diffusion dynamics of a concentrated aqueous ionic solution are presented. Previously, intensity level single frequency vibrational echo peak shift data for a concentrated NaCl solution showed that salt slows the spectral diffusion of the water's hydroxyl stretching vibration relative to that of pure water [56,58]. Spectral diffusion is related to how fast a molecular system undergoes structural fluctuations under a thermal equilibrium condition. The relationship between the vibrational echo observables and the microscopic dynamics of a system can be described by a frequency-frequency correlation function (FFCF). Spectral diffusion is observed as a change in peak shape of the 2D-IR vibrational echo spectra as a function of T_w [46,76]. It has been observed that spectral diffusion dynamics of water are slower when the size of hydrogen bond network is reduced by encapsulating water molecules in nanoscopic environments [55,58] and hydrogen bond network is disrupted significantly by dissolved ions [59]. To investigate hydrogen bond dynamics of water around ions, 2D-IR vibrational echo spectroscopy was performed on OD stretching vibration in a high concentration of NaBr solution with 5% of HOD in H_2O. The concentration was set so that there were four water molecules per ion on average (see Sec. 3.3). At this very high concentration the hydrogen bond network is disrupted. There is essentially no bulk water in which there is an extended network of interconnected water molecules. Basically, all water molecules are hydrogen bonded to ions. The question of the dynamics of the structural evolution of hydrogen bonds under these extreme conditions is addressed with the 2D-IR vibrational echo experiments.

4.1. Linear FT-IR absorption spectra

FT-IR absorption spectra of 5% HOD in neat water and NaBr:H_2O = 1:8 solution are shown in Fig. 4. The peaks at 2510 and 2540 cm^{-1} in FT-IR spectra are OD stretching vibrational mode in the neat water and the NaBr salt solution, respectively. It is known for neat water that the broad spectrum is caused by different numbers and different strengths of the hydrogen bonds [77]. More hydrogen bonds and stronger hydrogen bonds red shift the absorption, while few hydrogen bonds and weaker hydrogen bonds blue shift the absorption [16,17,43]. FT-IR spectrum of the OD stretching vibration in the NaBr solution is blue-shifted by $\sim$ 30 m^{-1} compared with that of neat water. The width of the neat water band is also somewhat wider, $\sim$ 160 cm^{-1} vs. $\sim$ 140 cm^{-1} for the salt solution. The salt solution line is still very broad, indicating a wide distribution of OD-ion interactions. In neat water, a blue shift is associated with weaker and/or fewer hydrogen bonds. However, the spectrum of the salt solution arises from a very different type of interaction. The hydroxyl group is mainly interacting with an ion rather than with another water molecule. Therefore, it is not safe to assume that the blue shift should be associated with weaker hydrogen bonding. Water molecules are hydrogen-bonded to ions by three ion-dipole interactions in HOD-Br^-, DOH-Br^-, and HDO-Na^+. The last two configurations have less influence on the OD stretching vibration.

4.2. 2D-IR vibrational echo spectra

2D-IR vibrational echo spectra of the OD stretching vibration in the NaBr solution are shown in Fig. 5 for a series of T_ws. The nature of the spectral peaks was discussed in

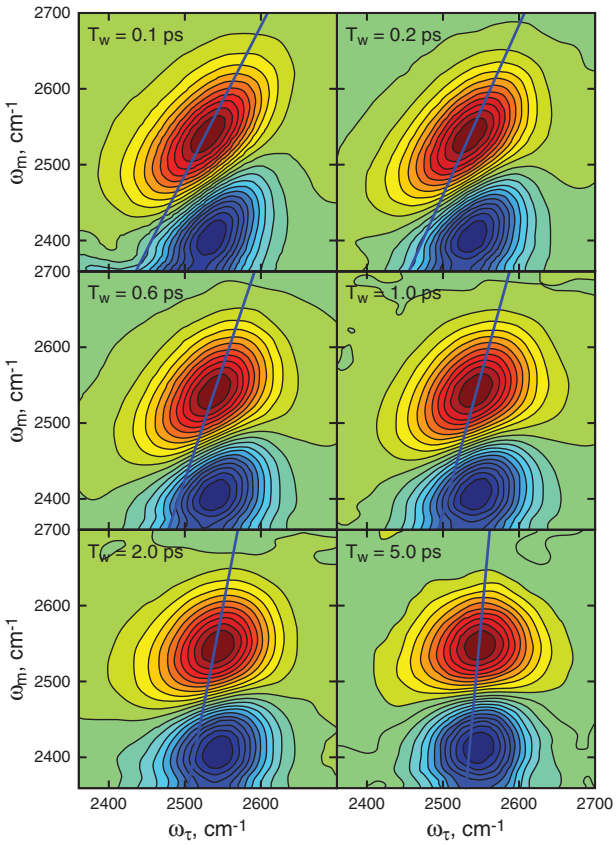

Figure 5 (online color at www.lphys.org) 2D-IR vibrational echo spectra of the OD stretching vibration obtained for the NaBr solution at increasing T_ws. Straight lines in the 2D spectra are the center lines defined in connection with the discussion of Fig. 6

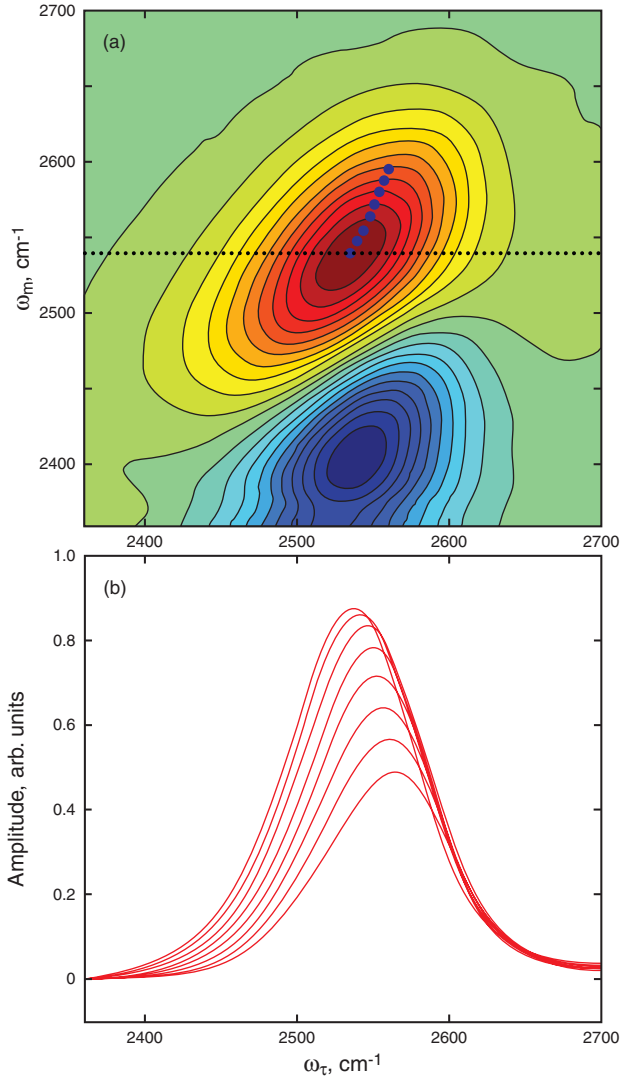

Figure 6 (online color at www.lphys.org) (a) – 2D-IR spectrum at $T_w = 0.2$ ps. A dotted horizontal line defines a frequency slice at $\omega_m = 2540$ cm^{-1} along the ω_τ axis. This slice gives the left most spectrum in (b). (b) – frequency slice spectra at different ω_m. The peak positions are obtained by fitting each to a Gaussian function. ω_m increases from left to right. Peak positions are marked with blue dots in (a). The center line slope (CLS) is obtained by a linear fit to the peak positions (blue dots) in (a)

Sec. 3.3. As shown in Sec. 2, 2D vibrational echo spectra are frequency correlation maps between the evolution (first coherence) and detection (second coherence) periods. The ω_τ axis is the axis of the initial frequencies at which the molecules are excited while the ω_m axis is the axis for the final frequencies at which the molecules emit the vibrational echo. The molecules are labeled with the initial frequencies along the ω_τ axis. The labeled molecules spectrally diffuse (move in the frequency domain) during the waiting time, T_w. The final frequencies of the labeled molecules are recorded along the ω_m axis. 2D-IR vibrational echo spectra show how the molecules move from the initial (ω_τ) to the final (ω_m) frequencies as a function of the waiting time, T_w.

Looking in particular at the fundamental transition (0-1 transition, red positive peak), a noticeable feature of 2D correlation spectra shown in Fig. 5 is a change of peak shape as T_w increases. The red peak is highly elongated along the diagonal at $T_w = 0.1$ ps. (The diagonal lines are not shown in Fig. 5. The blue lines are discussed below. See Fig. 3 for and example of the diagonal.) As T_w increases the shape changes and the band becomes more symmetrical. This change is the signature of spectral diffusion. In the long time limit, all structural configurations are sampled and, therefore, all frequencies are sampled. The band would become completely symmetrical. However, because of the overlap with the negatively going band that arises from emission at the 1-2 transition frequency, the bottom of the 0-1 band is eaten away. The shape of the band also has a T_w independent contribution. As discussed in detail below, ultrafast fluctuations produce a motionally

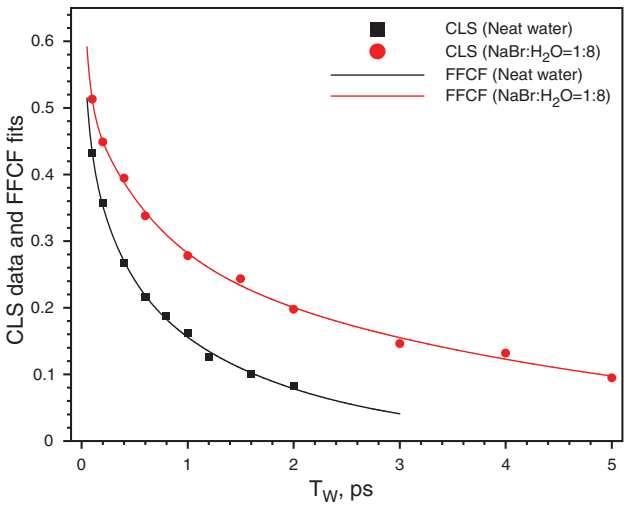

Figure 7 (online color at www.lphys.org) CLS plots (dots) vs. T_w for neat water and the NaBr solution. Solid lines are the fits to the CLS, which give the FFCFs for the two samples (see text)

narrowed (homogeneous) component of both 2D spectrum as well as the linear absorption spectrum. The motionally narrowed contribution produces a width along the ω_τ axis even at $T_w = 0$ ps. Although T_w independent, the motionally narrowed Lorentzian contribution to the 2D line shape can be determined by the procedure described in the next section.

4.3. The FFCF and the center line slope method

The frequency-frequency correlation function (FFCF) connects the experimental observables to the underlying dynamics. The FFCF is the probability that an oscillator with an initial frequency has the same frequency at time t later, averaged over all starting frequencies. It is generally written in terms of changes in frequency rather than the absolute frequency. Once the FFCF is known, all linear and nonlinear optical experimental observables can be calculated by time-dependent diagrammatic perturbation theory [46,76,78]. Conversely, the FFCF can be extracted from 2D vibrational echo spectra with input from the linear absorption. Generally, to determine the FFCF from 2D and linear spectra, full calculations of linear and nonlinear third-order response functions based on the time-dependent diagrammatic perturbation theory are performed iteratively until the calculation results converge to the experimental results. Here, a simpler method is introduced and used to determine the FFCF by circumventing the iterative fitting of the response functions. The inverse of the center line slope (CLS) of a 2D vibrational echo spectrum is defined as a new experimental observable to quantify spectral diffusion dynamics of water in bulk and in NaBr solution.

Fig. 6 illustrates how to define the CLS. A slice at a frequency ω_m (2540 cm^{-1}) along the ω_τ axis is marked as a dotted horizontal line in Fig. 6a. The projection of this slice onto the ω_τ axis is a spectrum. This particular slice is the left most spectrum in Fig. 6b. The peak position of the frequency slice can be obtained by fitting the frequency slice to a Gaussian or other appropriate function. The shape of the slice is not important. It is only necessary to determine its peak frequency. Frequency slices at different ω_m frequencies are shown in Fig. 6b, and their peak positions are marked with blue dots in Fig. 6a. The center line slope is obtained by plotting the ω_τ peak positions vs. ω_m. The "center lines" are shown as the blue lines in Fig. 5. The important feature of the center line is that as T_w increases, the slope becomes greater. In the limit of complete spectral diffusion, the long time limit, the 2D spectrum is symmetrical and the center line is vertical. In the other limit, $T_w = 0$ ps, and in the absence of a motionally narrowed component, the 2D spectrum is a thin line along the diagonal. The center line would be at 45°. As discussed below, the FFCF is related to the inverse of the center line slope. The inverse of the CLS has a maximum value of 1 at $T_w = 0$ ps and goes to 0 in the long time limit. The $T_w = 0$ ps maximum value of 1 can only occur in the absence of a motionally narrowed component. The larger the motionally narrowed contribution to the line shape is, the smaller the initial value of the inverse of the center line slope will be. The plot of the inverse of the CLS (simply referred to as the CLS for the remainder of this paper) vs. T_w is shown in Fig. 7 for both neat water and the NaBr solution. The decay of the CLS for the salt solution is considerably slower than that of bulk water.

In a subsequent publication, it will be shown theoretically that the CLS is the T_w dependent part of the FFCF to second order in time [79]. It will also be shown that the errors in determining the FFCF from the CLS arising from treating the problem to only second order are small. Furthermore, it is also possible to obtain the T_w independent part of the FFCF (the Lorentzian component) by combining the CLS and the linear absorption line shape [79].

The linear absorption spectrum $\sigma(\omega)$ can be calculated by a Fourier transformation of the linear response function $R^{(1)}(t)$,

$$\sigma(\omega) = \mathrm{Re}\left[\int_0^\infty dt \exp(i\omega t) R^{(1)}(t)\right] , \tag{12}$$

$$R^{(1)}(t) = \tag{13}$$

$$= |\mu_{01}|^2 \exp\left[-i\langle\omega_{01}\rangle t - g(t) - \frac{t}{2T_1} - \frac{t}{3T_{or}}\right] ,$$

where μ_{01} is the transition dipole moment of the fundamental transition (0-1), $\langle\omega_{10}\rangle$ is the ensemble-average of the fundamental transition frequency, and the population relaxation and orientational relaxation are included phe-

nomenologically with time constants T_1 and T_{or}, respectively. The line shape function $g(t)$ is defined as

$$g(t) = \int_0^t d\tau_2 \int_0^{\tau_2} d\tau_1 \, \langle \delta\omega_{10}(\tau_1)\delta\omega_{10}(0)\rangle \, , \qquad (14)$$

where $\langle \delta\omega_{10}(t)\delta\omega_{10}(0)\rangle$ is the FFCF, $C(t)$, for the 0-1 transition, which can be written in terms of the Kubo model as [80]

$$C(t) = \langle \delta\omega_{10}(t)\delta\omega_{10}(0)\rangle = \sum_i \Delta_i^2 \exp(-t/\tau_i) \, , \qquad (15)$$

where Δ_i and τ_i are the amplitudes and correlation times, respectively, of the various contributions to the frequency fluctuations. In the motionally narrowed limit (fast modulation limit) $\Delta\tau \ll 1$. In this limit, Δ and τ cannot be determined independently, but $T_2^* = (\Delta^2\tau)^{-1}$ or $\Gamma^* = (\pi T_2^*)^{-1}$ is the single parameter describing the motionally narrowed Lorentzian contribution to the line shape. T_2^* is the pure dephasing that gives rise to the pure homogeneous linewidth, Γ^*. Including contributions from population relaxation and orientational relaxation, the total dephasing time T_2 is

$$\frac{1}{T_2} = \frac{1}{T_2^*} + \frac{1}{2T_1} + \frac{1}{3T_{or}} \, , \qquad (16)$$

where $\Gamma = (\pi T_2)^{-1}$ is the Lorentzian homogeneous line width. If there is only a single term in Eq. (15) and it is motionally narrowed, the absorption line will be a Lorentzian and its line width yields T_2. In general, there are additional terms in $C(t)$, and the absorption line is inhomogeneously broadened. In this case, the FFCF cannot be determined from the absorption spectrum, and requires the 2D-IR vibrational echo experiment to measure the spectral diffusion and to obtain the FFCF.

The FFCFs, $C(t)$, of the OD stretching vibration for neat water and the NaBr solution are determined by using the FT-IR linear spectra shown in Fig. 4 and the CLSs in Fig. 7 without resorting to a full calculation of nonlinear response functions based on time-dependent diagrammatic perturbation theory [79]. For neat water, $C(t)$ has been found previously to be the sum of three terms [17,43],

$$C(t) = \Delta_1^2 \exp(-t/\tau_1) + \qquad (17)$$
$$+\Delta_2^2 \exp(-t/\tau_2) + \Delta_3^2 \exp(-t/\tau_3) \, .$$

By inserting Eq. (17) into Eq. (14), the corresponding line shape function is obtained as

$$g(t) = \Delta_1^2\tau_1^2[\exp(-t/\tau_1) + t/\tau_1 - 1] + \qquad (18)$$
$$+\Delta_2^2\tau_2^2[\exp(-t/\tau_2) + t/\tau_2 - 1] +$$
$$+\Delta_3^2\tau_3^2[\exp(-t/\tau_3) + t/\tau_3 - 1] \, .$$

The linear absorption spectrum $\sigma(\omega)$ can be calculated from Eq. (12) with Eqs. (13) and (18).

sample	Γ^*, cm^{-1}	Δ_2, cm^{-1}	τ_2, ps	Δ_3, cm^{-1}	τ_3, ps
water	34	43	0.3	52	1.5
water/NaBr	29	37	0.6	44	4.4

Table 1 Frequency-frequency correlation function parameters

The full procedure for using the CLS to obtain the FFCF, including discussions of approximations and errors, will be described in detail subsequently [79]. Very briefly, the CLS data points in Fig. 7 were fit to a bi-exponential function. The fits are shown as the lines in Fig. 7. These fits determine parameters Δ_2, τ_2, Δ_3, and τ_3. The two time constants are accurate [79]. However, the values of the Δ_i are floors to the true values. For a τ_i greater than ~ 10 times the FID half width, the associated Δ_i has little error. This is the situation with water for the slowest component of the FFCF. Furthermore, it has been shown that the floor for Δ_i associated with faster τ_i is 70% of the true value. Then, the only unknown parameters are Δ_2 and T_2. Using the three known parameters, the absorption line shape is fit, using the 70% floor for Δ_2, which determines Δ_2 and T_2. (For a motionally narrowed component, $g(t)$ can be written in terms of the single parameter T_2 for that component.) In general, T_2 can be separated into the three contributions, pure dephasing T_2^*, population relaxation T_1, and orientational T_{or}, by using pump-probe experiments to measure T_1 and T_{or}. However, in water, T_2^* is ~ 100 times larger than the other two contributions, and T_1 and T_{or} are ignored here. They will be reported in a subsequent publication [79]. The FFCF parameters for neat water and the NaBr solution are given in Table 1. The neat water parameters are almost the same as those reported previously [17], and the experimental results used to determine them here are more extensive.

4.4. Hydrogen bond dynamics of neat water and NaBr solution

A water molecule can be a hydrogen bond donor and acceptor at the same time [77]. In liquid water, the water molecule can form up to four hydrogen bonds in a tetrahedral geometry with neighboring water molecules making an extended hydrogen bond network. The hydrogen bond network fluctuates and evolves continuously under a thermal equilibrium condition. Hydrogen bonds form and break. Strong (short) bonds become weak (long), and vice versa. In the NaBr solution there are only four water molecules per negative ion and four water molecules per positive ion. It seems reasonable to assume that all water molecules in the NaBr solution are in hydration shells around ions. Given the ratio of ions to water molecules, there is no bulk water. Water molecules in NaBr solution are bound (or hydrogen-bonded) to ions by ion-dipole interaction and the water-ion structure evolves in time as

evidenced by the spectral diffusion. The linear absorption spectra shown in Fig. 4 shows that water in the salt solution is distinct from bulk water.

As shown in Table 1, the FFCF of OD stretching vibration is characterized by a motionally narrowed component, a subpicosecond intermediate component, and a slowest time component on a picosecond time scale. The motionally narrowed terms are reported as the pure homogeneous line width $\Gamma^* = \Delta_1^2\tau_1/\pi$. For neat water, molecular dynamics simulations and experiments show that the ultrafast motionally narrowed component arises from very local fluctuations in the hydrogen bond length with small contributions from angular changes [17,43,64,65,71,73]. The slowest, 1.5 ps component arises from global hydrogen bond structural rearrangements that randomize the hydrogen bond network. The two components (i.e. intermediate and slowest components) of the FFCF that are not motionally narrowed should be view as a model for a non-exponential decay. The intermediate component is a transition between the very local ultrafast single hydrogen bond fluctuations and the global complete randomization of the network.

In comparing the FFCF for the NaBr solution to that of neat water, the motionally narrowed components are similar. The amplitudes, Δ_2 and Δ_3 are also similar, although all are smaller for the NaBr solution. The large differences are in the time constants, τ_2 and τ_3, which are a factor of 2 and 3 longer respectively in the NaBr solution. This means that the time scale for complete randomization of the structure is much slower in the salt solution.

With only four water molecules per ion, the structural of water in the NaBr solution will have little resemblance to that of bulk water. Water molecules form hydration shells solvating ions in the NaBr solution by ion-dipole interaction and will have interactions like HOD-Br^-, DOH-Br^-, and HDO-Na^+. The dynamics will involve rearrangements of water molecules in relation to the ions rather than the water-water hydrogen bond rearrangements that occur in neat water. MD simulations performed on aqueous NaCl solutions at various concentrations of NaCl indicate that hydrogen bond structural relaxation slows down with increasing ion concentrations [81].

Recently, MD simulations were performed on a diluted I^-/HOD/D_2O system with a single iodide ion and 215 D_2O [82]. The results showed that the longest time component in the FFCF of OD stretching vibration was associated with the escape time of HOD from the first solvation shell of iodide ion to bulk. However, this simulation is not a model for a concentrated salt solution in which there is no bulk water. Furthermore, it does not give information on how water molecules solvating cations (Na^+) contribute to the overall hydrogen bond dynamics of water around ions, nor how the dynamics of water molecules that may bridge two anions or an anion and cation influence the spectral diffusion.

Bakker and coworkers performed two-color IR pump-probe experiments by pumping OH stretching vibration of DOH in D_2O salt solutions (6 M NaCl, NaBr, or NaI) near the center frequency of the OH absorption band and probing population relaxations at different frequencies [59,83]. It was observed that the decays of pump-probe signals got faster when the probing frequency moved away from the pumping frequency. The results were discussed in terms of a correlation time constant τ_c for spectral diffusion of the OH stretching vibration. A two Brownian oscillator model was necessary to extract the information from these indirect experiments and produced results that the correlations times were 20 to 30 times longer than that of neat water. The model used considered water bound to ions and water that was bulk like. These very long correlations times are in contrast to the measurements reported here in which the spectral diffusion components increase by factors of 2 and 3 compared to neat water.

Given the small number of water molecules per ion, it seems clear that the nature of water dynamics in concentrated salt solutions is fundamentally different from the dynamics of pure water. The inhomogeneous absorption spectrum must be composed of different configurations of a small number of water molecules associated with ions with few bulk-like water-water hydrogen bonds. The spectral diffusion is most likely associated with the structural rearrangements of water molecules strongly interacting with one or more ions and cannot involve exchange between a water-ion interaction and water in bulk. MD simulations will need to properly model the small numbers of waters per ion found in concentrated salt solutions.

5. Concluding remarks

The 2D-IR vibrational echo experimental method was described in considerable detail. 2D-IR vibrational echo spectroscopy has been developed over the last decade and has been utilized to study spectral diffusion, chemical exchange, isomerization, and the structure and dynamics of biomolecules. Investigations of such systems have just begun, and a great increase in the understanding of the fast structural dynamics of complex molecular systems is in the offing. In addition, 2D-IR vibrational echo spectroscopy has the potential to be applicable to many other microscopic molecular events occurring on subpicosecond and picosecond time scales.

In this paper, both the theoretical and experimental underpinnings of ultrafast 2D-IR vibrational echo spectroscopy were reviewed. In addition, a new method for extracting the frequency-frequency correlation function from T_w dependent 2D spectra was presented. The center line slope method makes it possible to obtain the FFCF without iterative fitting of the 2D spectra using time dependent perturbation theory techniques. As will be shown in a subsequent publication, the CLS method produces results that are not distorted by finite bandwidth of the excitation pulses or apodization procedures [79]. In addition, the first 2D-IR vibrational echo measurements of water spectral diffusion in a concentrated salt solution were presented. It was found that the structural randomization of the system

is significantly slower than in pure water. Additional experiments on concentrated salt solutions will be reported in a subsequent publication. The dynamics of water in a variety of types of salt solutions over a range of concentrations are currently being studied.

Acknowledgements This work was supported by grants from the Air Force Office of Scientific Research (F49620-01-1-0018), the National Science Foundation (DMR-0332692), the Department of Energy (DE-FG03-84ER13251), and the National Institutes of Health (2 R01 GM-061137-05).

References

[1] T. Brixner, J. Stenger, H.M. Vaswani, M. Cho, and G.R. Fleming, Nature **34**, 625–628 (2005).
[2] J. Zheng, K. Kwak, J.B. Asbury, X. Chen, I. Piletic, and M.D. Fayer, Science **309**, 1338–1343 (2005).
[3] Y.S. Kim and R.M. Hochstrasser, Proc. Natl. Acad. Sci. USA **102**, 11185–11190 (2005).
[4] J. Zheng, K. Kwak, J. Xie, and M.D. Fayer, Science **313**, 1951–1955 (2006).
[5] R.R. Ernst, G. Bodenhausen, and A. Wokaun, Principles of Nuclear Magnetic Resonance in One and Two Dimensions (Oxford University Press, Oxford, 1987).
[6] D. Zimdars, A. Tokmakoff, S. Chen, S.R. Greenfield, M.D. Fayer, T.I. Smith, and H.A. Schwettman, Phys. Rev. Lett. **70**, 2718–2721 (1993).
[7] J. Zheng, K. Kwak, and M.D. Fayer, Acc. Chem. Res. **40**, 75–83 (2007).
[8] I.J. Finkelstein, J. Zheng, H. Ishikawa, S. Kim, K. Kwak, and M.D. Fayer, Phys. Chem. Chem. Phys. **9**, 1533–1549 (2007).
[9] M.C. Asplund, M.T. Zanni, and R.M. Hochstrasser, Proc. Natl. Acad. Sci. USA **97**, 8219–8224 (2000).
[10] M.T. Zanni, M.C. Asplund, and R.M. Hochstrasser, J. Chem. Phys. **114**, 4579–4590 (2001).
[11] M.T. Zanni and R.M. Hochstrasser, Curr. Opin. Struct. Biol. **11**, 516–522 (2001).
[12] J.B. Asbury, T. Steinel, C. Stromberg, K.J. Gaffney, I.R. Piletic, A. Goun, and M.D. Fayer, Chem. Phys. Lett. **374**, 362–371 (2003).
[13] J.B. Asbury, T. Steinel, C. Stromberg, K.J. Gaffney, I.R. Piletic, A. Goun, and M.D. Fayer, Phys. Rev. Lett. **91**, 237402 (2003).
[14] M. Khalil, N. Demirdöven, and A. Tokmakoff, Phys. Rev. Lett. **90**, 047401 (2003).
[15] M. Khalil, N. Demirdöven, and A. Tokmakoff, J. Phys. Chem. A **107**, 5258–5279 (2003).
[16] J.B. Asbury, T. Steinel, and M.D. Fayer, J. Lumin. **107**, 271–286 (2004).
[17] J.B. Asbury, T. Steinel, K. Kwak, S.A. Corcelli, C.P. Lawrence, J.L. Skinner, and M.D. Fayer, J. Chem. Phys. **121**, 12431–12446 (2004).
[18] N. Demirdöven, C.M. Cheatum, H.S. Chung, M. Khalil, J. Knoester, and A. Tokmakoff, J. Am. Chem. Soc. **126**, 7981–7990 (2004).
[19] Y.S. Kim, J. Wang, and R.M. Hochstrasser, J. Phys. Chem. B **109**, 7511–7521 (2005).
[20] J. Zheng, K. Kwak, T. Steinel, J.B. Asbury, X. Chen, J. Xie, and M.D. Fayer, J. Chem. Phys. **123**, 164301 (2005).
[21] K. Kwak, J. Zheng, H. Cang, and M.D. Fayer, J. Phys. Chem. B **110**, 19998–20013 (2006).
[22] J.J. Loparo, S.T. Roberts, and A. Tokmakoff, J. Chem. Phys **125**, 194521 (2006).
[23] J.J. Loparo, S.T. Roberts, and A. Tokmakoff, J. Chem. Phys **125**, 194522 (2006).
[24] J. Zheng, K. Kwak, X. Chen, J.B. Asbury, and M.D. Fayer, J. Am. Chem. Soc **128**, 2977–2987 (2006).
[25] I.J. Finkelstein, H. Ishikawa, S. Kim, A.M. Massari, and M.D. Fayer, Proc. Nat. Acad. Sci. USA **104**, 2637–2642 (2007).
[26] J.B. Asbury, T. Steinel, C. Stromberg, K.J. Gaffney, I.R. Piletic, and M.D. Fayer, J. Chem. Phys. **119**, 12981–12997 (2003).
[27] M. Khalil, N. Demirdöven, and A. Tokmakoff, J. Chem. Phys. **121**, 362–373 (2004).
[28] L.P. DeFlores, Z. Ganim, S.F. Ackley, H.S. Chung, and A. Tokmakoff, J. Phys. Chem. B **110**, 18973–18980 (2006).
[29] J.B. Asbury, T. Steinel, and M.D. Fayer, Chem. Phys. Lett. **381**, 139–146 (2003).
[30] P. Mukherjee, I. Kass, I.T. Arkin, and M.T. Zanni, Proc. Natl. Acad. Sci. USA **103**, 3528–3533 (2006).
[31] J. Wang, J. Chen, and R.M. Hochstrasser, J. Phys. Chem. B **110**, 7545–7555 (2006).
[32] H.S. Chung, M. Khalil, A.W. Smith, Z. Ganim, and A. Tokmakoff, Proc. Natl. Acad. Sci. USA **102**, 612–617 (2005).
[33] S. Woutersen, R. Pfister, P. Hamm, Y. Mu, D.S. Kosov, and G. Stock, J. Chem. Phys. **117**, 6833–6840 (2002).
[34] Y. Kim and R.M. Hochstrasser, J. Phys. Chem. B **109**, 6884–6891 (2005).
[35] C. Fang and R.M. Hochstrasser, J. Phys. Chem. B **109**, 18652–18663 (2005).
[36] P. Mukherjee, A.T. Krummel, E.C. Fulmer, I. Kass, I.T. Arkin, and M.T. Zanni, J. Chem. Phys. **120**, 10215–10224 (2004).
[37] M.F. DeCamp, L. DeFlores, J.M. McCracken, A. Tokmakoff, K. Kwac, and M. Cho, J. Phys. Chem. B. **109**, 11016–11026 (2005).
[38] S. Mukamel and D. Abramavicius, Chem. Rev. **104**, 2073–2098 (2004).
[39] J.H. Choi, H. Lee, K.K. Lee, S. Hahn, and M. Cho, J. Chem. Phys. **126**, 045102–045114 (2007).
[40] A.M. Massari, I.J. Finkelstein, and M.D. Fayer, J. Am. Chem. Soc. **128**, 3990–3997 (2006).
[41] I.J. Finkelstein, A.M. Massari, and M.D. Fayer, Biophys. J. **92**, 3652–3662 (2007).
[42] A.M. Massari, B.L. McClain, I.J. Finkelstein, A.P. Lee, H.L. Reynolds, K.L. Bren, and M.D. Fayer, J. Phys. Chem. B **110**, 18803–18810 (2006).
[43] J.B. Asbury, T. Steinel, C. Stromberg, S.A. Corcelli, C.P. Lawrence, J.L. Skinner, and M.D. Fayer, J. Phys. Chem. A **108**, 1107–1119 (2004).
[44] O. Golonzka, M. Khalil, N. Demirdöven, and A. Tokmakoff, Phys. Rev. Lett. **86**, 2154–2157 (2001).
[45] O. Golonzka, M. Khalil, N. Demirdöven, and A. Tokmakoff, J. Chem. Phys. **115**, 10814–10828 (2001).
[46] S. Mukamel, Principles of Nonlinear Optical Spectroscopy (Oxford University Press, New York, 1995).

[47] J. Sung and R.J. Silbey, J. Chem. Phys. **115**, 9266–9287 (2001).
[48] D.M. Jonas, Annu. Rev. Phys. Chem. **54**, 425–463 (2003).
[49] R. Trebino, K.W. DeLong, D.N. Fittinghoff, J.N. Sweetser, M.A. Krumbugel, B.A. Richman, and D.J. Kane, Rev. Sci. Instr. **69**, 3277–3295 (1997).
[50] J.D. Hybl, Y. Christophe, and D.M. Jonas, Chem. Phys. **266**, 295–309 (2001).
[51] J.D. Hybl, A.A. Ferro, and D.M. Jonas, J. Chem. Phys. **115**, 6606–6622 (2001).
[52] T. Brixner, T. Mancal, I.V. Stiopkin, and G.R. Fleming, J. Chem. Phys **121**, 4221–4236 (2004).
[53] S. Woutersen, U. Emmerichs, and H. J. Bakker, Science **278**, 658-660 (1997).
[54] T. Steinel, J.B. Asbury, J.R. Zheng, and M.D. Fayer, J. Phys. Chem. A **108**, 10957–10964 (2004).
[55] H.-S. Tan, I.R. Piletic, and M.D. Fayer, J. Chem. Phys. **122**, 174501–174509 (2005).
[56] H.-S. Tan, I.R. Piletic, R.E. Riter, N.E. Levinger, and M.D. Fayer, Phys. Rev. Lett. **94**, 057405 (2005).
[57] I.R. Piletic, H.-S. Tan, and M.D. Fayer, J. Phys. Chem. B **109**, 21273–21284 (2005).
[58] I. Piletic, D.E. Moilanen, D.B. Spry, N.E. Levinger, and M.D. Fayer, J. Phys. Chem. A **110**, 4985–4999 (2006).
[59] M.F. Kropman and H.J. Bakker, J. Chem. Phys. **115**, 8942–8948 (2001).
[60] M.F. Kropman and H.J. Bakker, Science **291**, 2118–2120 (2001).
[61] M.F. Kropman, H.-K. Nienhuys, S. Woutersen, and H.J. Bakker, J. Phys. Chem. A **105**, 4622–4626 (2001).
[62] J. Stenger, D. Madsen, J. Dreyer, P. Hamm, E.T.J. Nibbering, and T. Elsaesser, Chem. Phys. Lett. **354**, 256–263 (2002).
[63] J. Stenger, D. Madsen, P. Hamm, E.T.J. Nibbering, and T. Elsaesser, J. Phys. Chem. A. **106**, 2341–2350 (2002).
[64] C.J. Fecko, J.D. Eaves, J.J. Loparo, A. Tokmakoff, and P.L. Geissler, Science **301**, 1698–1702 (2003).
[65] C.J. Fecko, J.J. Loparo, S.T. Roberts, and A. Tokmakoff, J. Chem. Phys. **122**, 054506–054518 (2005).
[66] R. Rey, K.B. Moller, and J.T. Hynes, J. Phys. Chem. A **106**, 11993–11996 (2002).
[67] C.P. Lawrence and J.L. Skinner, J. Chem. Phys. **117**, 8847–8854 (2002).
[68] A. Piryatinski and J.L. Skinner, J. Phys. Chem. B **106**, 8055–8063 (2002).
[69] A. Piryatinski, C.P. Lawrence, and J.L. Skinner, J. Chem. Phys. **118**, 9672–9679 (2003).
[70] C.P. Lawrence and J.L. Skinner, Chem. Phys. Lett. **369**, 472–477 (2003).
[71] C.P. Lawrence and J.L. Skinner, J. Chem. Phys. **118**, 264–272 (2003).
[72] S. Corcelli, C.P. Lawrence, and J.L. Skinner, J. Chem. Phys. **120**, 8107–8117 (2004).
[73] S.A. Corcelli, C.P. Lawrence, J.B. Asbury, T. Steinel, M.D. Fayer, and J.L. Skinner, J. Chem. Phys. **121**, 8897–8900 (2004).
[74] R. Rey, K.B. Moller, and J.T. Hynes, Chem. Rev. **104**, 1915–1928 (2004).
[75] K. Moller, R. Rey, and J. Hynes, J. Phys. Chem. A **108**, 1275–1289 (2004).
[76] S. Mukamel, Ann. Rev. Phys. Chem. **51**, 691–729 (2000).
[77] G.C. Pimentel and A.L. McClellan, The Hydrogen Bond (W.H. Freeman and Co., San Francisco, 1960).
[78] W.M. Zhang, V. Chernyak, and S. Mukamel, J. Chem. Phys. **110**, 5011–5028 (1999).
[79] K. Kwak, S. Park, I.J. Finkelstein, and M.D. Fayer, J. Chem. Phys., in preparation.
[80] R. Kubo, in: D. Ter Haar (ed.), Fluctuation, Relaxation, and Resonance in Magnetic Systems (Oliver and Boyd, London, 1961).
[81] A. Chandra, Phys. Rev. Lett. **85**, 768–771 (2000).
[82] B. Nigro, S. Re, D. Laage, R. Rey, and J.T. Hynes, J. Phys. Chem. A **110**, 11237–11243 (2006).
[83] S. Woutersen and H.J. Bakker, Phys. Rev. Lett. **83**, 2077–2080 (1999).